Surface dependence of CO 2 adsorption on Zn 2GeO 4

ARTICLE *in* LANGMUIR · JUNE 2012

Impact Factor: 4.46 · DOI: 10.1021/la301679h · Source: PubMed

6 AUTHORS, INCLUDING:

li Liu
Beijing Normal University
40 PUBLICATIONS **251** CITATIONS
SEE PROFILE

Weiliu Fan
Shandong University
79 PUBLICATIONS **1,439** CITATIONS
SEE PROFILE

Xian Zhao
Shandong University
239 PUBLICATIONS **2,030** CITATIONS
SEE PROFILE

Pan Li
Hebei Normal University
24 PUBLICATIONS **298** CITATIONS
SEE PROFILE

Langmuir

Article

pubs.acs.org/Langmuir

Surface Dependence of CO_2 Adsorption on Zn_2GeO_4

Li Liu,[†] Weiliu Fan,*[,‡] Xian Zhao,*[,†] Honggang Sun,[†] Pan Li,[†] and Liming Sun[†]

[†]State Key Laboratory of Crystal Materials and [‡]Department of Chemistry and Chemical Engineering, Shandong University, Jinan, 250100, China

Supporting Information

ABSTRACT: An understanding of the interaction between Zn_2GeO_4 and the CO_2 molecule is vital for developing its role in the photocatalytic reduction of CO_2. In this study, we present the structure and energetics of CO_2 adsorbed onto the stoichiometric perfectly and the oxygen vacancy defect of Zn_2GeO_4 (010) and (001) surfaces using density functional theory slab calculations. The major finding is that the surface structure of the Zn_2GeO_4 is important for CO_2 adsorption and activation, i.e., the interaction of CO_2 with Zn_2GeO_4 surfaces is structure-dependent. The ability of CO_2 adsorption on (001) is higher than that of CO_2 adsorption on (010). For the (010) surface, the active sites $O_{2c}\cdots Ge_{3c}$ and $Ge_{3c}-O_{3c}$ interact with the CO_2 molecule leading to a bidentate carbonate species. The presence of $Ge_{3c}-O_{2c}\cdots Ge_{3c}$ bonds on the (001) surface strengthens the interaction of CO_2 with the (001) surface, and results in a bridged carbonate-like species. Furthermore, a comparison of the calculated adsorption energies of CO_2 adsorption on perfect and defective Zn_2GeO_4 (010) and (001) surfaces shows that CO_2 has the strongest adsorption near a surface oxygen vacancy site, with an adsorption energy −1.05 to −2.17 eV, stronger than adsorption of CO_2 on perfect Zn_2GeO_4 surfaces (E_{ads} = −0.91 to −1.12 eV) or adsorption of CO_2 on a surface oxygen defect site (E_{ads} = −0.24 to −0.95 eV). Additionally, for the defective Zn_2GeO_4 surfaces, the oxygen vacancies are the active sites. CO_2 that adsorbs directly at the Vo site can be dissociated into CO and O and the Vo defect can be healed by the oxygen atom released during the dissociation process. On further analysis of the dissociative adsorption mechanism of CO_2 on the surface oxygen defect site, we concluded that dissociative adsorption of CO_2 favors the stepwise dissociation mechanism and the dissociation process can be described as $CO_2 + Vo \rightarrow CO_2^{\delta-}/Vo \rightarrow CO_{adsorbed} + O_{surface}$. This result has an important implication for understanding the photoreduction of CO_2 by using Zn_2GeO_4 nanoribbons.

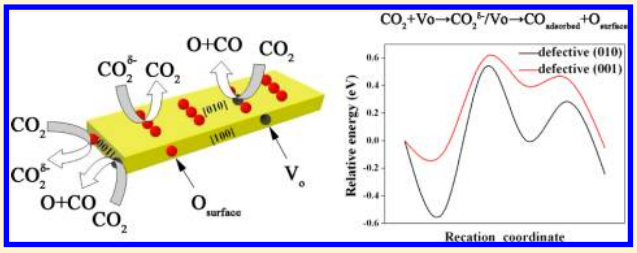

1. INTRODUCTION

It is known that the shape of a nanocatalyst tremendously affects reaction performance.[1] It has been verified that adsorption and activation of reactants as well as desorption of the products are strongly dependent on the surface atomic arrangement. In other words, the morphology of nanocatalysts as determined by the exposed specific crystal facets could considerably modify the reaction performance.[2−6]

Carbon dioxide (CO_2) is the chief greenhouse gas that results from human activities and causes global warming and climate change.[7,8] Conversion of CO_2 into hydrocarbon fuel using solar energy has great significance in coping with the problems of global warming and energy shortage.[9−11]

Semiconductor-mediated photocatalytic reduction has received a lot of attention with regard to its potential applications in clean energy and environmental cleanup, for example, in the photoreduction of CO_2 to CH_4 and the photocatalytic degradation of pollutants in water and air.[12,13] The first report about photocatalytic reduction of CO_2 to formaldehyde, formic acid, methanol, and methane as main products over suspending semiconductor particles in water was published by Fujishima and his co-workers in 1979.[14] Since then, many efforts have been devoted to developing efficient photocatalysts for the reduction of CO_2 in water.[9,15]

Zinc orthogermanate (Zn_2GeO_4), as a ternary oxide, showed good activity for water splitting, degradation of pollutants, and photoreduction of CO_2. It also exhibits high-wavelength selectivity in UV photodetectors with fast response and recovery time, and bright white-bluish luminescence.[9,16] Recently, well-designed single-crystalline Zn_2GeO_4 nanobelts have been found to be photocatalysts that greatly improve the photocatalytic activity toward reduction of CO_2 into renewable hydrocarbon fuel (CH_4) in the presence of water vapor.[9] The rate of this photocatalytic reaction can be controlled by several steps: photoexcitation of the Zn_2GeO_4 surface, creating electron−hole pairs, followed by their transfer to CO_2 and H_2O. However, the detailed mechanism is not well understood. Furthermore, the kind of surface structure that strengthens the interaction of CO_2 with Zn_2GeO_4 surfaces is unknown. Therefore, identifying the mechanism and the effect of surface structure on CO_2 adsorption and activation would represent a significant advance in the understanding of CO_2 photoreduction, and also has important significance for developing better photocatalysts.

Received: October 6, 2011
Revised: June 10, 2012
Published: June 14, 2012

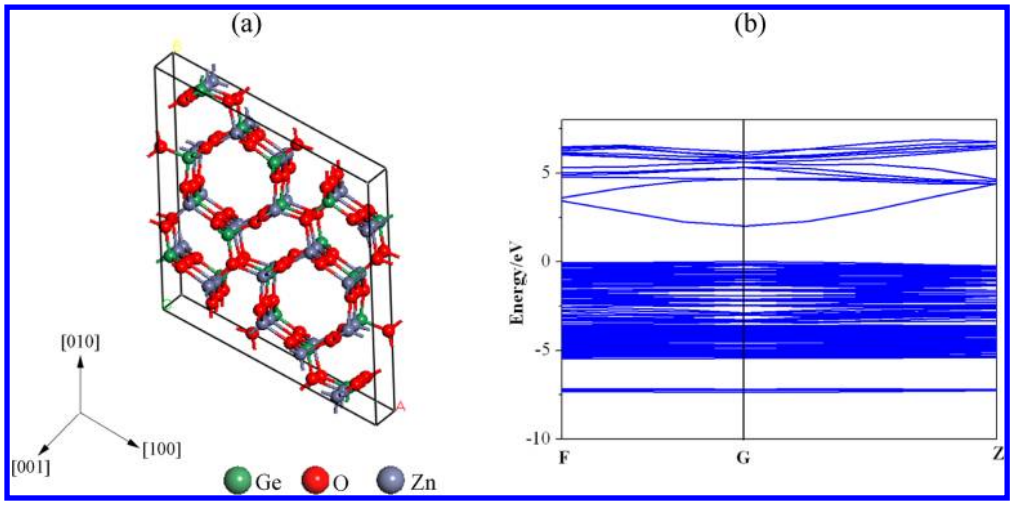

Figure 1. (a) Unit cell of Zn_2GeO_4 and (b) band structure for Zn_2GeO_4.

Over the past few decades, there have been extensive studies dedicated toward understanding the fundamentals of CO_2−surface interactions, including different modes, structure of adsorbed CO_2, and charge transfer behavior.[17−21] Nonetheless, only a few theoretical calculations about how surface structures affect photocatalysts have been reported. Theoretical understanding of the influence of photocatalyst surface structure is extremely important to design and synthesize novel photocatalysts. In the present work, the structure sensitivity of Zn_2GeO_4 was studied by examining the adsorption of CO_2 on perfect and oxygen vacancy defect Zn_2GeO_4 (010) and (001) surfaces. It was shown that Zn_2GeO_4 surfaces are indeed active for CO_2 activation and this reaction is structure-sensitive. A variety of possible binding configurations of CO_2 on the perfect and defective Zn_2GeO_4 (010) and (001) surfaces in terms of geometries, energies, and net charges were explored. The bonding mechanisms of CO_2 on these surfaces were also discussed with examination of the local density of states (LDOS) for the adsorbed CO_2. We anticipate that results from the study of CO_2 adsorption on the perfect and defective Zn_2GeO_4 (010) and (001) surfaces will allow us to understand in great detail the chemistry of the Zn_2GeO_4 surfaces. The paper is organized as follows: in section 2, we describe the computational methods and models; in section 3, we present and discuss the results. Our conclusions are given in section 4.

2. COMPUTATIONAL METHODS AND SURFACE MODELS

Density functional theory (DFT)[22] with a GGA-PW91[23,24] functional, as implemented in the program CASTEP,[25] was used for all the calculations. Electronic wave functions were expanded in a plane wave basis set, and ionic cores were described by ultrasoft pseudopotentials.[26] A 340 eV plane wave basis set the cutoff, and the cutoff energy was used throughout our calculations. The Monkhorst-Pack[27] grids of 3 × 3 × 3 *k*-points were used for the bulk unit cell, 2 × 1 × 1 and 2 × 2 × 1 *k*-points for the (010) surface and (001) surface, respectively. Our test calculations with Monkhorst-Pack grids of 3 × 2 × 1 and 3 × 3 × 1 gave almost the same geometries and adsorption energies as with the Monkhorst-Pack grids of 2 × 1 × 1 and 2 × 2 × 1 for the (010) surface and (001) surface, respectively. Also, in order to determine accurate activation barriers of the reaction, we chose the complete LST/QST approach to search for transition states of the reactions.[28]

Experimental work[9] showed that the Zn_2GeO_4 nanoribbon is a uniform single crystal with the longitudinal direction along [001] and the width direction along [100]. The two major exposed surfaces of the nanobelts are {010} facets. In principle, the crystallographic surfaces (100) and (010) of the rhombohedral Zn_2GeO_4 are equivalent. Therefore, two surfaces of Zn_2GeO_4 were considered in this work, the (010) and (001) planes. Among them, the (010) surface has several different terminations. They can expose 1-fold-coordinated O, 2-fold-coordinated O, 3-fold-coordinated O, 2-fold-coordinated Ge, 3-fold-coordinated Ge, 2-fold-coordinated Zn, and 3-fold-coordinated Zn atoms. In the present work, the (010) surface was terminated by exposing 2-fold-coordinated O, 3-fold-coordinated O, 3-fold-coordinated Ge, and 3-fold-coordinated Zn. This is clearly the most favorable cleavage, since it only breaks 9 bonds against 15 or 18 for the cleavages in other ways. For three-dimensional periodic boundary conditions, a surface is represented by a slab, which is separated from its images in the direction perpendicular to the surface by a vacuum gap. In this work, we constructed stoichiometric slabs of 9.656 Å × 14.487 Å × 8.209 Å (seven atomic layers) and 14.487 Å × 14.487 Å × 6.696 Å (five atomic layers) with a vacuum thickness of 12 Å to model the (010) and (001) of Zn_2GeO_4, respectively. In all calculations, the atoms in the bottom layers were fixed, but the atoms in the three topmost layers, as well as C and O atoms in CO_2, were allowed to relax. The geometry of the isolated CO_2 molecule was optimized using a large cell of 10 Å × 10 Å × 10 Å. The calculated C−O bond length and O−C−O angle were equal to 1.18 Å and 180.0°, and were in good agreement with the experimental values of 1.17 Å and 180.0°,[29] respectively. After optimization, the local density of states (LDOS) and Mulliken charge analysis[30] were performed. These analyses were used to help understand the nature of the bonding and the interaction between CO_2 and the Zn_2GeO_4 surfaces.

The adsorption energy was defined as

$$E_{ads} = E(CO_2/slab) - [E(CO_2) + E(slab)]$$

where the first term is the total energy of the slab with the adsorbed CO_2 on the surface, the second term is the total energy of free CO_2, and the third term is the total energy of the bare slab of the surface. According to the above definitions, a negative E_{ads} value corresponds to an exothermic adsorption, and the more negative the E_{ads}, the stronger the adsorption.

3. RESULTS AND DISCUSSION

In Figure 1a, the rhombohedral phase of Zn_2GeO_4 unit cell is shown. To test the accuracy of our approach, we compared the optimized unit cell parameters obtained using PW91 with the experimental value and other GGA methods (PBE and rPBE). As shown in Table 1, the optimized unit cell parameters at the PW91 level are $a = b = 14.486$ Å, $c = 9.656$ Å, $\alpha = \beta = 90.0°$, and $\gamma = 120.0°$, which approach the experimental values[9] more closely than the PBE and rPBE levels. Figure 1b shows the

dx.doi.org/10.1021/la301679h | *Langmuir* 2012, 28, 10415−10424

Table 1. Calculated and Experimental Lattice Parameters of Zn_2GeO_4

computing methods	$A = b$ (Å)	c (Å)	$\alpha = \beta$ (deg)	γ (deg)
PW91	14.486	9.656	90.0	120.0
PBE	14.513	9.678	90.0	120.0
rPBE	14.624	9.754	90.0	120.0
Experiment[a]	14.230	9.530	90.0	120.0

[a]See ref 9.

calculated band structure using GGA-PW91. The band gap of Zn_2GeO_4 is estimated to be 2.0 eV, which is smaller than UV−vis spectra results (4.5 eV).[9] Such an underestimation is a usual problem of the GGA functional.[31−33] However, for surface adsorption calculations, the GGA is preferable. This is because the surface adsorption processes involve bond breaking and/or bond formation, and there is direct evidence that in some cases GGA gives better adsorption energies for molecules.[23,34,35] For these reasons, in the following sections only GGA-PW91 energies are used in the discussion.

3.1. Structure of the Zn_2GeO_4 Surfaces. The surface energies and structures of the Zn_2GeO_4 (010) surface were first studied using slabs of seven (9.656 Å × 14.487 Å × 8.209 Å), eight (9.656 Å × 14.487 Å × 9.631 Å), and nine (9.656 Å × 14.487 Å × 11.254 Å) atomic layers thickness, and the (001) surface using slabs of five (14.487 Å × 14.487 Å × 6.696 Å), seven (14.487 Å × 14.487 Å × 9.833 Å), and nine (14.487 Å × 14.487 Å × 13.027 Å) atomic layers, maintaining the stoichiometric balance. The surface energy was calculated using the equation $S = (E^N_{slab} - NE_{bulk})/2A$, where A is the area of the surface, E^N_{slab} is the total energy of the surface slabs, N is the number of Zn_2GeO_4 units in the cell, and E_{bulk} is the energy per stoichiometric unit of the bulk. For a slab whose top and bottom surfaces are not equivalent, the surface energy of the slab is given by $S = (E^N_{slab} - NE_{bulk})/A - S_{bottom}$. The S_{bottom} was calculated by using a slab which has identical termination on both sides of the slab without surface relaxation. The results of our present surface energy calculations are summarized in Table 2. It was found that the (010) surface had a lower surface

Table 2. Calculated Zn_2GeO_4 Surface Energies

surface plane	layer	surface energy (J/m^2)
(010)	7	2.13
	8	2.14
	9	2.11
(001)	5	2.66
	7	2.70
	9	2.74

energy, and the (001) surface had a higher surface energy, which explains why the (010) face is the natural cleavage surface and the (001) face is the natural growth surface in Zn_2GeO_4 nanobelts. The data in Table 2 show that the surface energies of (010) converged to within 0.01−0.03 J/m^2, the surface energies of (001) converged to within 0.04−0.08 J/m^2, indicating that seven layers for (010) and five layers for (001) are thick enough in calculated models. Therefore, to keep the computational cost low, we only chose these slabs to study CO_2 adsorption in the present work.

Figure 2 shows the structure of the Zn_2GeO_4 (010) and (001) surfaces after relaxation. On these surfaces, 3-fold-coordinated germanium (Ge_{3c}), 3-fold-coordinated zinc (Zn_{3c}),

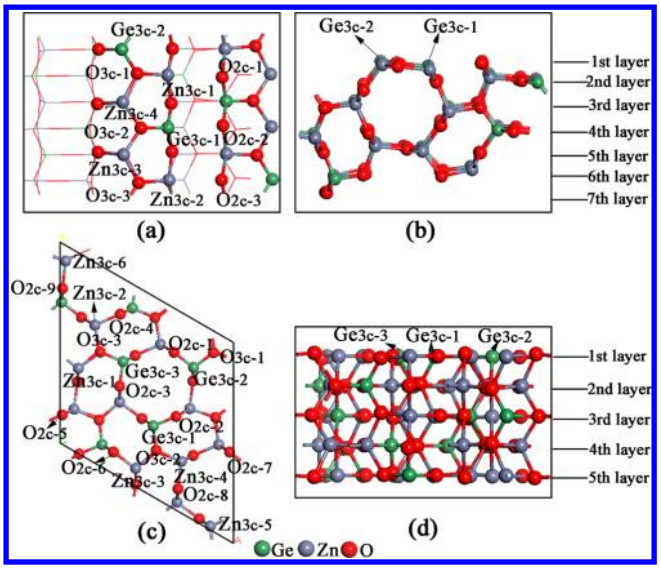

Figure 2. Top (left) and side (right) views of the Zn_2GeO_4 (010) and (001) surfaces.

3-fold-coordinated oxygen (O_{3c}), and 2-fold-coordinated oxygen (O_{2c}) atoms are exposed, among which, Ge_{3c}, Zn_{3c}, and O_{2c} are coordinately unsaturated. Both surfaces consist of metal (Zn and Ge) and oxygen atoms, but they differ in surface structure and composition. For example, both surfaces have M_{3c}−O_{3c} and $M_{3c}\cdots O_{2c}$ (M = Zn or Ge) bonds; among them, the M_{3c}−O_{3c} bond originated from the bulk Zn_2GeO_4, whereas the $M_{3c}\cdots O_{2c}$ bond represents the interaction between the M_{3c} and the O_{2c} of the exposed Zn_2GeO_4 surfaces. However, the (010) surface has O_{3c}−$M_{3c}\cdots O_{2c}$ bonds, while the (001) surface not only has O_{3c}−$M_{3c}\cdots O_{2c}$ bands, but also possesses the Ge_{3c}−$O_{2c}\cdots Ge_{3c}$ bond. This means they will have similarities and differences for CO_2 adsorption and activation.

The top views of the Zn_2GeO_4 (010) and (001) surfaces are used to label the surface atoms. When this involves more than one of the same types of atom, it is distinguished by adding an additional subscript. For example, $Ge_{3c\text{-}1}$ represents the first 3-fold-coordinated Ge atom on the Zn_2GeO_4 surface, $Ge_{3c\text{-}2}$ represents the second 3-fold-coordinated Ge atom on the Zn_2GeO_4 surface, and the rest may be deduced by analogy.

The Zn_2GeO_4 surface remains stable in the full-geometry optimization. In Table 3 are listed the vertical displacements of the surface atoms relative to their bulk positions that have been calculated from the equilibrium slab geometry, and the notation of the atoms follows that in Figure 2. The data in Table 3 show that the main displacements are the surface metal atoms, while the vertical shifts of oxygen atoms are much smaller. For example, for the Zn_2GeO_4 (010) surface, the Zn_{3c} atoms considerably relax outward by 0.282−0.471 Å, the Ge_{3c} atoms move inward by 0.173−0.308 Å, the under-coordinated O_{2c} atoms move outward by 0.008−0.111 Å, while the $O_{3c\text{-}1}$, $O_{3c\text{-}2}$, and $O_{3c\text{-}3}$ relax −0.185, −0.162, and 0.016 Å, respectively. This indicates that the Zn_2GeO_4 surface remains stable in the full-geometry optimization.

3.2. CO_2 Adsorption on Perfect Zn_2GeO_4 Surfaces. To correlate surface structures with photocatalytic activity, interaction between CO_2 molecule and the surface of the Zn_2GeO_4 photocatalyst was examined. For clarity, the two oxygen atoms of the adsorbed CO_2 were labeled as O_a and O_b if they are not in equivalent positions. Five models were

dx.doi.org/10.1021/la301679h | Langmuir 2012, 28, 10415−10424

Table 3. Comparison of the Vertical Relaxation of the Top Surface Atoms for the Bare (010) and (001) Surfaces of Zn_2GeO_4

	z-shifts, Å												
surface	$Zn_{3c\text{-}1}$	$Zn_{3c\text{-}2}$	$Zn_{3c\text{-}3}$	$Zn_{3c\text{-}4}$	$Ge_{3c\text{-}1}$	$Ge_{3c\text{-}2}$	$Ge_{3c\text{-}3}$	$O_{2c\text{-}1}$	$O_{2c\text{-}2}$	$O_{2c\text{-}3}$	$O_{3c\text{-}1}$	$O_{3c\text{-}2}$	$O_{3c\text{-}3}$
(010)	0.282	0.365	0.471	0.380	−0.173	−0.308	—	0.008	0.013	0.111	−0.185	−0.162	0.016
(001)	−0.153	−0.309	−0.164	−0.158	−0.297	−0.301	0.334	0.002	−0.102	0.004	0.396	0.406	0.265

constructed to determine the adsorption energy of the system (see Figure 3). The first one is a linearly adsorbed model where

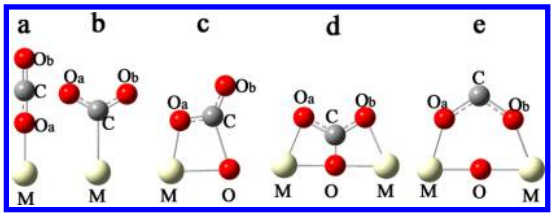

Figure 3. Possible configurations of adsorbed CO_2 on the Zn_2GeO_4 surface.

the CO_2 molecule adsorbs via the O_a atom to the surface as shown in Figure 3a. The second is a C-absorbed model absorbed via the C atom to form a monodentate carbonate species as shown in Figure 3b. In the third, a CO_2 molecule interacts with the surface via both the O_a and C atom generating a bidentate carbonate species as shown in Figure 3c. The fourth has a bridged carbonate geometry with two O atoms of CO_2 binding with two metal atoms and the C atom of CO_2 pointing downward and forming a C···O bond with the O atom on the surface (Figure 3d). The fifth has a bridging configuration with two O atoms of CO_2 binding with two metal atoms and the C atom of CO_2 pointing upward (Figure 3e). The formation of the fourth or the fifth model requires the presence of an M−O···M bond on the surface.

We optimized each CO_2-adsorbed structure and obtained the adsorption energy of the system and found that CO_2 adsorbed on (010) surface of the third model was the most stable, while CO_2 adsorbed on (001) surface of the fourth model was most stable. Taking the (010) surface, for example, (the different binding configurations of adsorbed CO_2 on the (010) and (001) surfaces are provided in Supporting Information), the very low adsorption energy of only 0.02 to −0.20 eV for the adsorbed CO_2 with the linearly adsorbed model and the C-absorbed model indicates that these interactions with the surface are weak, while the adsorption energy with the bidentate carbonate model is −0.12 to −1.04 eV. In fact, previous work has demonstrated that CO_2 adsorbed on pure metal or metal compounds surface with these models are the most stable.[17,18,36] In this study, the focus is on surface dependence of CO_2 adsorption on Zn_2GeO_4, and therefore, these two models were chosen to study the effect of surface structure and active sites on it.

The adsorption of CO_2 on the perfect Zn_2GeO_4 (010) surface was first studied. Various sites on the Zn_2GeO_4 (010) surface, including the $Ge_{3c\text{-}1}$, $Ge_{3c\text{-}2}$, $Zn_{3c\text{-}1}$, $Zn_{3c\text{-}2}$, $Zn_{3c\text{-}3}$, $Zn_{3c\text{-}4}$, $Ge_{3c\text{-}1}\cdots O_{2c\text{-}2}$, $Ge_{3c\text{-}1}-O_{3c\text{-}2}$, $Ge_{3c\text{-}2}-O_{3c\text{-}1}$, $Zn_{3c\text{-}1}\cdots O_{2c\text{-}1}$, $Zn_{3c\text{-}1}-O_{3c\text{-}1}$, $Zn_{3c\text{-}2}\cdots O_{2c\text{-}3}$, $Zn_{3c\text{-}2}-O_{3c\text{-}3}$, $Zn_{3c\text{-}3}-O_{3c\text{-}2}$, $Zn_{3c\text{-}3}-O_{3c\text{-}3}$, $Zn_{3c\text{-}4}-O_{3c\text{-}1}$, and $Zn_{3c\text{-}4}-O_{3c\text{-}2}$ sites, were explored for CO_2 adsorption. From the above models, the two most stable configurations (010, 1) and (010, 2) were obtained. The optimized structures and key structural parameters are given in Figure S1 (see Supporting Information), and the other less stable configurations are provided in Figure S2. The adsorption energies (E_{ads}) as well as other structural parameters of those configurations are shown in Table S1. In configuration (010, 1), CO_2 was adsorbed across the $Ge_{3c\text{-}1}-O_{3c\text{-}2}$ bridge site as a bidentate carbonate species. The C atom of CO_2 is bonded to the surface $O_{3c\text{-}2}$ atom, while O_a of CO_2 is bonded to the surface $Ge_{3c\text{-}1}$ atom. The distances of the newly formed $O_a-Ge_{3c\text{-}1}$ and $C-O_{3c\text{-}2}$ bonds are 1.817 Å and 1.390 Å, respectively. The adsorption energy of CO_2 in (010, 1) is −0.91 eV. In configuration (010, 2), CO_2 adsorbs at the $Ge_{3c\text{-}1}\cdots O_{2c\text{-}2}$ bridge site, generating another bidentate carbonate species. The C atom is bonded to the surface $O_{2c\text{-}2}$ atom, whereas O_a is bonded to the surface $Ge_{3c\text{-}1}$ atom. The distances of the newly formed $O_a-Ge_{3c\text{-}1}$ and $C-O_{2c\text{-}2}$ bonds are 1.835 Å and 1.439 Å, respectively. The adsorption energy of CO_2 in (010, 2) is −1.04 eV. As shown in Table S1, the adsorbed CO_2 in (010, 1) and (010, 2) are greatly distorted from a gas-phase CO_2 molecule. Both the $C-O_a$ and $C-O_b$ bonds are stretched, and the O_a-C-O_b angle is decreased to 122.2−124.8°, and the elongated C−O bonds and reduced O_a-C-O_b angle indicate that the adsorbed CO_2 is activated.[17,19]

Next, CO_2 adsorption on the perfect Zn_2GeO_4 (001) surface was studied. A number of different adsorption sites were also explored. The configuration (001, 1) was found to be most stable for CO_2 adsorption on the Zn_2GeO_4 (001) surface, as shown in Figure S1, and the other less stable configurations are provided in Figure S3. The adsorption energy (E_{ads}) and structural parameters are listed in Table S1. In (001, 1), the CO_2 with two O atoms bridging two 3-fold Ge atoms ($Ge_{3c\text{-}1}$, $Ge_{3c\text{-}2}$) and C atom pointing downward and forming a C···O bond with the 2-fold O atom ($O_{2c\text{-}2}$) on the surface forms a bridged carbonate-like species. The distances of the newly formed $C-O_{2c\text{-}2}$, $O_a-Ge_{3c\text{-}1}$, and $O_b-Ge_{3c\text{-}2}$ bonds are 1.351 Å, 1.932 Å, and 2.076 Å, respectively. The adsorption energy of CO_2 in (001, 1) is −1.12 eV. For the configuration (001, 1), the O_a-C-O_b angle (125.9°) is considerably reduced from the value 180.0° corresponding to the linear gas-phase CO_2 molecule. In addition, the $C-O_a$ distance is significantly increased to 1.323 Å and the $C-O_b$ distance is increased to 1.253 Å compared to 1.180 Å for the free molecule. These structural data strongly suggest that the adsorbed CO_2 is highly activated.

In addition, the adsorption of CO and atomic oxygen at the same time on perfect Zn_2GeO_4 (010) or (001) surfaces were also calculated. It was found that CO and atomic oxygen recombined to $CO_2^{\delta-}$ again after optimization, and this result suggests that CO_2 spontaneous dissociation on perfect Zn_2GeO_4 surfaces is not possible.

For decades, the Mulliken charge analysis has been widely used, since the Mulliken charges are readily available from orbital-based ab initio calculations, although the Mulliken charge analysis has some disadvantages because of its weak theoretical basis. However, the Mulliken population analysis is still a useful tool for describing bond strength and charge changes.[30,37] In this study, the Mulliken charge analysis was performed to understand the charge redistribution upon CO_2

dx.doi.org/10.1021/la301679h | Langmuir 2012, 28, 10415−10424

adsorption. The net charges for the isolated CO_2 molecule and different CO_2 adsorption configurations on Zn_2GeO_4 surfaces are given in Table S1. The results clearly show that the adsorbed CO_2 molecules are partially negatively charged (−0.36 to −0.41 |e|), indicating that CO_2 accepted electrons from the surface and formed a partially and negatively charged $CO_2^{\delta-}$ species. This negatively charged $CO_2^{\delta-}$ intermediate has also been described in experimental[38,39] and theoretical work.[20,21]

Local density of states (LDOS) analyses was also performed to aid in the understanding of the interaction between adsorbed CO_2 and the surface. Figure S4a shows the LDOS plots of the C and O_a (or O_b) atoms of a free CO_2 molecule. In the free CO_2 molecule, the highest occupied molecular orbital (HOMO) is the $1\pi_g$ bonding orbital, which is situated on oxygen atoms, while the lowest unoccupied molecular orbital (LUMO) is the $2\pi_u$ antibonding orbital, which is situated on the carbon atom and two oxygen atoms.[19,29] The HOMO $1\pi_g$ orbital of free CO_2 is at the Fermi level, while the bands of the adsorbed CO_2 in (010, 1), (010, 2), and (001, 1) clearly shift downward (b and c in Figure S4). In addition, upon activation, as shown in Figure S4b and S4c, the C−O (O_{2c} or O_{3c}) bond was clearly formed, as indicated by the significant overlaps between the C and surface O (O_{2c} or O_{3c}) atoms orbital. Also, in all configurations, the LDOS clearly shows stronger interaction between the O_a (or O_b) atoms and the surface Ge_{3c} atoms, which corresponds to the binding of CO_2 with the Zn_2GeO_4 surfaces.

The present results show a strong surface dependence for the interaction of CO_2 with Zn_2GeO_4 surfaces. From the interaction energies presented in Table S1, it is clear that bridged carbonate species on the (001) surface is more stable than the bidentate carbonate species on the (010) surface. The bond distance of C−O (surface O) in the bridged carbonate species (1.351 Å) was relatively shorter than that of the bidentate carbonate species (1.390−1.439 Å); see Figure S1. The origin of the surface dependence can be understood by considering the different surface structures. The strong interaction between the (001) surface and the CO_2 molecule results in the formation of a bridged carbonate-like species. This requires the presence of the Ge_{3c}−O_{2c}···Ge_{3c} bond on the surface to interact with the C and two O atoms of the CO_2 molecule. Moreover, a comparison of the type of surface sites available at the Zn_2GeO_4 (010) and (001) surfaces shows that different surfaces have different active sites: the active sites are $Ge_{3c\text{-}1}$−$O_{3c\text{-}2}$ and $Ge_{3c\text{-}1}$···$O_{2c\text{-}2}$ on the (010) surface and Ge_{3c}−O_{2c}···Ge_{3c} on the (001) surface. In addition, the charge partitions between O_a and O_b in (001, 1) are significantly different from those in (010, 1), (010, 2). As shown in Table S1, O_b became more negative in (001, 1) than in (010, 1) and (010, 2), whereas O_a was less negative, while the C atom became more positive in (001, 1) than in (010, 1) and (010, 2). These results indicate that CO_2 adsorption and activation greatly depend on the surface structure of the Zn_2GeO_4. That is, different surface structures have different selectivities for CO_2 adsorption and activation. The above observations on structure sensitive adsorption behavior on perfect Zn_2GeO_4 surfaces also point to some interesting trends. We observed that surfaces with high surface energies, that is, the perfect (001) planes of Zn_2GeO_4 (S = 2.66 J/m^2) lead to a stronger adsorption of the adsorbate, as demonstrated by their high exothermic adsorption energies. These results are in agreement with earlier theoretical studies also suggesting that the interaction of CO_2 with Ni and Co surfaces is structure sensitive. Wang et al.[19] analyzed the adsorption of CO_2 on Ni (111), Ni (100), and Ni (110) surfaces and found that adsorption of CO_2 on Ni surfaces is structure-sensitive: CO_2 dissociates on Ni (110), whereas it is not activated on Ni (111) and exhibits both behaviors on the Ni (100) face. De la Pena O'Shea et al.[21] analyzed the CO_2 adsorption on Co (111), Co (110), and Co (100) surfaces and found that this adsorption is surface-sensitive and the CO_2 is activated by the Co (110) surface.

Zou and his co-workers[9] indicated that the two major exposed surfaces of the Zn_2GeO_4 nanobelts are (010) surfaces, with the width direction along (100) and the growth direction along (001) direction. It seems that the major exposed surface (010) may be the specific surface and act as the active sites for CO_2 photoreduction. However, the above calculation results prove that the perfect (001) surface is the specific surface and has a higher ability for CO_2 activation; in other words, the major exposed perfect (010) surfaces of the Zn_2GeO_4 nanobelts did not display the highest activity for CO_2 activation. This result appears to a certain extent to be inconsistent with experimental reports. Therefore, there must be other factors that have an effect on CO_2 adsorption and activation, among which the oxygen vacancy (Vo) is a common influencing factor. Oxygen vacancy is an intrinsic defect in metal oxides, which is the most reactive site on the surface and modifies the structure of the materials and changes the electronic and chemical properties of the surface.[40] Moreover, experimental and theoretical studies on the photoinduced activation of CO_2 all point to a role for oxygen vacancy.[41−44] For example, Indrakanti et al.[42] used DFT calculations to study the CO_2 adsorption on oxygen vacancies on TiO_2 surfaces and suggested that re-creation of the oxygen vacancy is a key step in the photocatalytic reduction of CO_2 on reduced TiO_2 surfaces. Therefore, in the following section we studied the effects of oxygen vacancy on CO_2 adsorption and activation on Zn_2GeO_4.

3.3. CO_2 Adsorption on Defective Zn_2GeO_4 Surfaces.

In this section, we explored CO_2 adsorption on the defective Zn_2GeO_4 surfaces with an oxygen vacancy. The surface oxygen vacancy on Zn_2GeO_4 was created by removing a surface O_{2c} or O_{3c} atom from the perfect surface. The original Ge_{3c} and Zn_{3c} atoms bound to the top O (O_{2c} or O_{3c}) atom at the vacancy site become 2-fold-coordinated, and are denoted as Ge_{3c}(d) and Zn_{3c}(d), respectively, as shown in Figure 4. In this figure, the location of Vo is indicated using a black sphere. The formation energy of an oxygen vacancy was defined with respect to the energy of an oxygen molecule in the triplet state and calculated

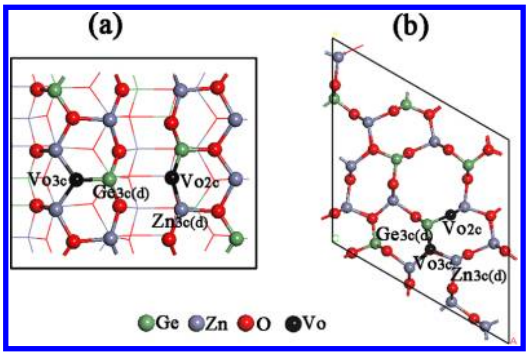

Figure 4. Different types of oxygen vacancies: (a) top view of Zn_2GeO_4 (010) surface; (b) top view of Zn_2GeO_4 (001) surface.

dx.doi.org/10.1021/la301679h | Langmuir 2012, 28, 10415−10424

according to $E_{Vo} = -(E_{perfect} - E_{defective} - 1/2\ E_{O2})$. Our calculated oxygen vacancy formation energies of Zn_2GeO_4 (010) and (001) surfaces are listed in Table S2. We note that the calculated oxygen vacancy formation energy of the (010) surface is slightly higher than of the (001) surface. Consequently, the density of oxygen vacancy is expected to be low on the (010) surface. However, to our knowledge, there is no experimental study about oxygen vacancy on Zn_2GeO_4 surfaces.

First, we considered the influence of nearby oxygen vacancy on the CO_2 adsorption configurations (010, 1), (010, 2), and (001, 1). Variations of the adsorption energies for these three configurations in the presence of a nearby oxygen vacancy defect were examined, and the most stable configuration is provided in Figure S5. We denote these configurations as D(010, 1), D(010, 2), D(001, 1). It was found that the presence of such surface vacancy can modify the energy for those configurations that adsorb CO_2 on the perfect surface at sites near the vacancy. From the data in Table S3, it can be seen that the presence of a Vo defect leads to a substantial increase in adsorption energies. For D(010, 1) and D(010, 2), the presence of the nearby defect site $Vo_{2c\text{-}1}$ can enhance the binding energies, increasing by 0.14 and 0.24 eV, respectively. For D(001, 1), the nearest $Vo_{3c\text{-}2}$ site was examined, and the calculated adsorption energy of CO_2 in this configuration was −2.17 eV. It is interesting to note that the charge transfer values in these configurations were slightly larger than those configurations that adsorb CO_2 on the perfect surface. These results suggest that the electron-rich defective Zn_2GeO_4 surfaces can help to stabilize the negatively charged $CO_2^{\delta-}$ species. Another interesting phenomenon is that the interaction of CO_2 with defective Zn_2GeO_4 surfaces still has a surface dependence in this case: the adsorption energy of D(001, 1) is higher than that of D(010, 1) and D(010, 2).

Generally, oxygen vacancies are also active sites on the surface of metal oxides. Therefore, in the following section we consider CO_2 adsorption at a surface oxygen defect site. The selective stable configurations are shown in Figure 5, labeled as (010, $Vo_{2c\text{-}2}$-B), (010, $Vo_{3c\text{-}1}$-L), (010, $Vo_{3c\text{-}1}$-D), (010, $Vo_{3c\text{-}2}$-B), and (001, $Vo_{3c\text{-}1}$-L). Among them, L represents a linearly adsorbed model (CO_2), while B is bent ($CO_2^{\delta-}$) and D is a dissociative adsorbed model (CO+O). A summary of the adsorption energies as well as other structural parameters of those configurations are presented in Table S3. When a CO_2 molecule adsorbs directly at the Vo site, a new dissociative adsorption configuration (010, $Vo_{3c\text{-}1}$-D) results as indicated in Figure 5. In (010, $Vo_{3c\text{-}1}$-D), CO_2 is dissociated into a CO_b adsorbed on the surface Zn atom and an O_a filling in the oxygen vacancy site. After CO_2 dissociative adsorption on the Vo site, the oxygen vacancy defect was found to be healed by the O_a, and this dissociative adsorbed model was equivalent to adsorption of CO on the perfect Zn_2GeO_4 surface. The adsorption energy of this configuration was −0.24 eV. In the case of (010, $Vo_{2c\text{-}2}$-B) and (010, $Vo_{3c\text{-}2}$-B), the O_a atom of the adsorbed CO_2 filled in the oxygen vacancy site and the C atom of the adsorbed CO_2 interacted with the surface Ge atom, forming the C−Ge bond. The adsorption energy was −0.95 eV for (010, $Vo_{2c\text{-}2}$-B) and −0.45 eV for (010, $Vo_{3c\text{-}2}$-B). For the other two configurations identified on the Vo site, CO_2 retained a near-linear structure with adsorption energies of −0.50 eV for (010, $Vo_{3c\text{-}1}$-L) and −0.60 eV for (001, $Vo_{3c\text{-}1}$-L). For (010, $Vo_{3c\text{-}1}$-L) and (001, $Vo_{3c\text{-}1}$-L), there were no covalent bonds formed between CO_2 and surface atoms, with the shortest

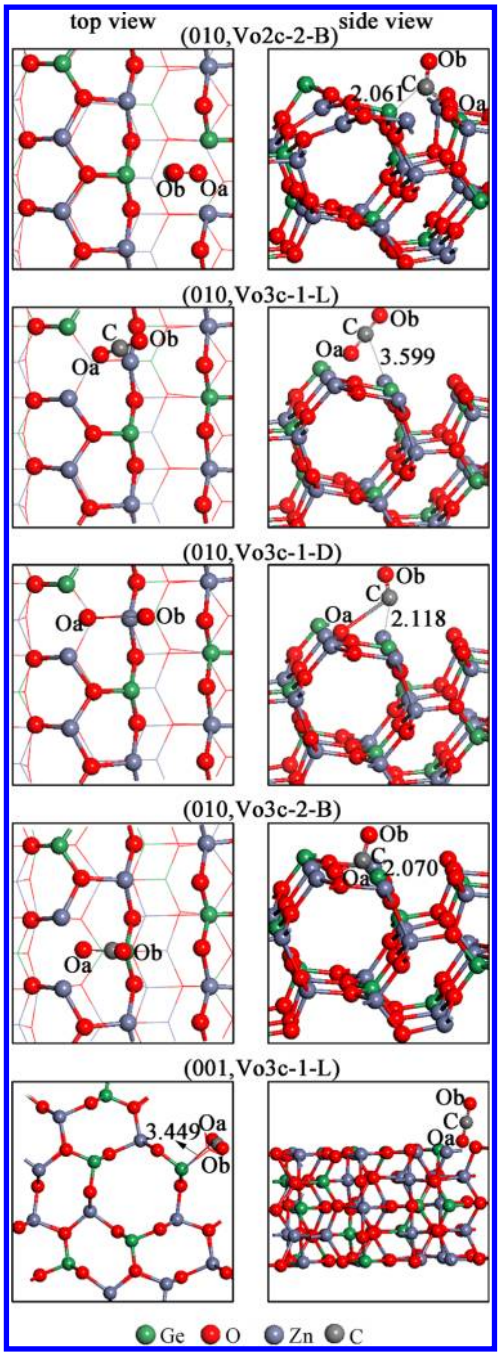

Figure 5. Optimized adsorption configurations of CO_2 at an oxygen vacancy defect on the Zn_2GeO_4 surfaces. Distances are in Å.

contacts (3.449−3.599 Å) being between surface metal atom (Ge or Zn) and the O_a or C atom of the CO_2 molecule (see Figure 5). According to the calculated energies and the adsorption configurations, it can be seen that the CO_2 molecule that adsorbs directly at the Vo site also has a surface dependence and the defective (001) surface would appear to have poorer activity than defective (010) surface. The favorable adsorption energies of configurations on the defective (001) surface are all linearly adsorbed models. In addition, the optimized largest dissociative adsorption energy of CO_2 at an oxygen vacancy defect on the (001) surface is −0.05 eV; see Supporting Information for the configuration (001, $Vo_{2c\text{-}5}$-D). These results suggest that dissociative adsorption CO_2 on a

dx.doi.org/10.1021/la301679h | Langmuir 2012, 28, 10415−10424

defective (001) surface is not energetically favorable compared to that on a defective (010) surface.

3.4. CO_2 Dissociative Adsorption Mechanism on the Defective Zn_2GeO_4 Surfaces. Having identified the favorable dissociated structures, we now explored the dissociative adsorption mechanism of CO_2 on defective Zn_2GeO_4 surfaces. The potential energy profiles for the dissociative adsorption of CO_2 on the Zn_2GeO_4 (010) surface with the $Vo_{3c\text{-}1}$ site are shown in Figure 6a. The structures of the transition states involved in this pathway are shown together with the potential energy profile. There are two possible reaction routes with regard to the dissociative adsorption of CO_2: the stepwise dissociation mechanism (black line) and the direct dissociation mechanism (red line). For the stepwise dissociation mechanism, the first step starts from (010, $Vo_{3c\text{-}1}$-L), with O_a by filling the vacancy and C bending toward the $Zn_{3c\text{-}1}(d)$ through the transition state TS1, which leads to a bent $CO_2^{\delta-}$ species in (010, $Vo_{3c\text{-}1}$-B). In TS1, the distance between C and $Zn_{3c\text{-}1}(d)$ decreased to 2.725 Å from 3.599 Å in (010, $Vo_{3c\text{-}1}$-L), the angle of CO_2 was 140.1°, and the C−O_a and C−O_b bond lengths were 1.308 and 1.190 Å, respectively. This step is endothermic by 0.51 eV, with a much higher activation barrier of 1.03 eV. In the second step, the bent $CO_2^{\delta-}$ species in (010, $Vo_{3c\text{-}1}$-B) dissociated into adsorbed CO_b and O_a atom in (10, $Vo_{3c\text{-}1}$-D) through the transition state TS2. In TS2, the C−O_a bond broke, the distance between C and O_a increased to 1.932 Å from 1.425 Å in (010, $Vo_{3c\text{-}1}$-B), the distance between C−$Zn_{3c\text{-}1}(d)$ bond decreased to 1.978 Å from 2.030 Å in (010, $Vo_{3c\text{-}1}$-B), and the C−O_b bond length was 1.152 Å. In (010, $Vo_{3c\text{-}1}$-D), the distance between C and O_a was 2.830 Å and the C−O_b bond length was 1.146 Å. The second step was largely exothermic, by 0.25 eV, and had a small activation barrier of 0.27 eV. The energy barrier of TS1 was higher than that of TS2. This indicates that the first step could be the rate-determining step in this stepwise dissociation process. For the direct dissociation mechanism from (010, $Vo_{3c\text{-}1}$-L), the molecularly adsorbed CO_2 dissociated into adsorbed CO_b and O_a atom through a transition state TS3, with a significantly high activation barrier of 1.76 eV. In TS3, the distance between C and $Zn_{3c\text{-}1}(d)$ decreased to 2.271 Å from 3.599 Å in (010, $Vo_{3c\text{-}1}$-L), the angle of CO_2 was 129.1°, the C−O_a and C−O_b bond lengths were 1.612 and 1.192 Å, respectively. The above results for CO_2 dissociated into adsorbed CO_b and O_a atom on defective Zn_2GeO_4 (010) show that the dissociative adsorption of CO_2 favors the stepwise dissociation mechanism, for which the rate-determining step is 1.03 eV lower than the barrier for the direct dissociation mechanism (1.76 eV).

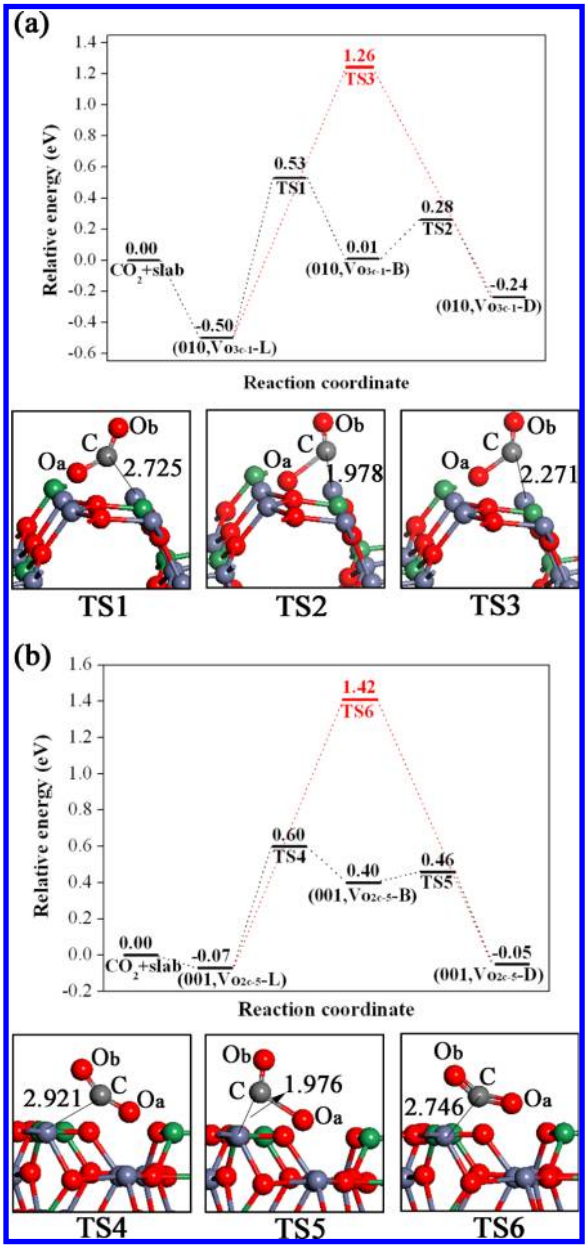

Figure 6. Potential energy profiles for the dissociation of CO_2 on the defective Zn_2GeO_4 (010) and (001) surfaces with oxygen vacancy site $Vo_{3c\text{-}1}$ and $Vo_{2c\text{-}5}$, respectively. Structures of the transition states are also shown. Distances are in Å. Relative energies are in eV.

Additionally, the dissociative adsorption mechanism of CO_2 on the defective Zn_2GeO_4 (001) surface with $Vo_{2c\text{-}5}$ is also given in Figure 6b. Comparison of the results of CO_2 dissociated into CO_b and O_a through stepwise dissociation path on the defective Zn_2GeO_4 surfaces show that the highest barrier and reaction energy for the conversion of CO_2 to (010, $Vo_{3c\text{-}1}$-D) with $Vo_{3c\text{-}1}$ were 1.03 and −0.24 eV, respectively, whereas those for the (001, $Vo_{2c\text{-}5}$-D) formation were 0.67 and −0.05 eV, respectively. As a result, the (010, $Vo_{3c\text{-}1}$-D) formation is thermodynamically preferred on the defective Zn_2GeO_4 surface with $Vo_{3c\text{-}1}$, whereas the (001, $Vo_{2c\text{-}5}$-D) formation is more kinetically favorable. These results indicate that the dissociation process of CO_2 on the defective Zn_2GeO_4 surfaces has a surface dependence.

Then, to better understand the interaction mechanism between CO_2 and oxygen vacancies on Zn_2GeO_4, we chose the defective Zn_2GeO_4 (010) surface with $Vo_{3c\text{-}1}$ to probe the stepwise dissociation mechanism of CO_2 by analyzing the local density of state (LDOS) and the electron charge density for the adsorption process of structure (010, $Vo_{3c\text{-}1}$-L), with a starting distance between C and $Zn_{3c\text{-}1}(d)$ of 3.599 Å. Figure 7a−c shows the LDOS and the charge density plots of each adsorbed CO_2 in the decomposition path: (a) (010, $Vo_{3c\text{-}1}$-L), (b) (010, $Vo_{3c\text{-}1}$-B), and (c) (010, $Vo_{3c\text{-}1}$-D). In the initial state (010, $Vo_{3c\text{-}1}$-L), the oxygen (O_a and O_b) states that were localized at about 5.0 eV below the Fermi level were the main contributor to the HOMO of the almost intact CO_2 molecule, and the LUMO of the intact CO_2 molecule mainly resulted from the carbon atom and were localized at about 2.5 eV beyond the Fermi level (see Figure 7a1). In the intermediate state (010, $Vo_{3c\text{-}1}$-B), the DOS projected on both the C and the O became

dx.doi.org/10.1021/la301679h | Langmuir 2012, 28, 10415−10424

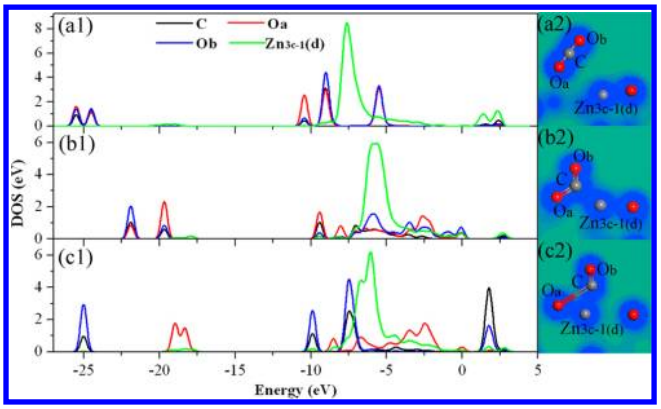

Figure 7. Local density of states (LDOS) and charge density plots for the dissociation of CO_2 on the defective Zn_2GeO_4 (010) surface with oxygen vacancy site $Vo_{3c\text{-}1}$: (a) (010, $Vo_{3c\text{-}1}$-L), (b) (010, $Vo_{3c\text{-}1}$-B), and (c) (010, $Vo_{3c\text{-}1}$-D). For charge density plots, a plane parallel to B and C axes was used for the cross section.

complex due to the obviously bent CO_2 structure and its interaction with the Zn_2GeO_4 (010) surface. Importantly, for the carbon and the oxygen, new occupied peaks exist in the energy range of −5.0 to 0 eV, which originated from the lowered LUMO of the activated CO_2 species. A Mulliken charge analysis showed that ∼0.86 electrons were transferred from the $Zn_{3c\text{-}1}(d)$ atoms to the CO_2 species. Consequently, the adsorbed CO_2 was significantly activated, and the strong C−$Zn_{3c\text{-}1}(d)$ interactions made the dissociation of the CO_2 adsorbate. In the final chemisorbed state (010, $Vo_{3c\text{-}1}$-D), the orbital mixing between C and O_b was observed at ∼2.5, −7.5, −10, and −25 eV, while the orbital of O_a almost completely separated in these places. As displayed in Figure 7c2, the interaction between the C and the O_a became very weak and there was almost no charge transfer between C and O_a. This result indicates that CO_2 has been reduced to CO. Upon dissociation, the O_a atom of the CO_2 molecule adsorbs at the Vo site where it heals the vacancy, while the CO_b adsorbs at the nearby metal atom, and therefore, the reduction process of CO_2 on the defective Zn_2GeO_4 (010) surface can be described by the following equation:

$$CO_2 + Vo \rightarrow CO_2^{\delta-}/Vo \rightarrow CO_{adsorbed} + O_{surface}$$

At this point, we carried out a detailed analysis of the interaction of CO_2 with the perfect and the defective Zn_2GeO_4 (010) and (001) surfaces by using DFT calculations. Our above results show that adsorption of CO_2 on both perfect and defective Zn_2GeO_4 surfaces is highly sensitive to the structure of the crystallographic plane: CO_2 was found to exhibit both activation and dissociation on defective Zn_2GeO_4 (010) and (001) surfaces, whereas it preferentially shows an activated adsorption on perfect Zn_2GeO_4 (010) and (001) surfaces. A comparison of the calculated adsorption energies of CO_2 adsorption on perfect and defective Zn_2GeO_4 (010) and (001) surfaces shows that CO_2 has strongest adsorption near a surface oxygen vacancy site, with an adsorption energy −1.05 to −2.17 eV, stronger than adsorption of CO_2 on perfect Zn_2GeO_4 surfaces (E_{ads} = −0.91 to −1.12 eV) or adsorption of CO_2 directly at a surface oxygen defect site (E_{ads} = −0.24 to −0.95 eV). Moreover, through analysis of the dissociative adsorption mechanism of CO_2 on defective Zn_2GeO_4 surfaces, we found that CO_2 dissociation on the defective Zn_2GeO_4 (010) surface was thermodynamically preferred and dissociation on the defective Zn_2GeO_4 (001) surface was kinetically preferred.

4. CONCLUSIONS

To contribute to the understanding of the mechanism of CO_2 adsorption on Zn_2GeO_4 surfaces, we have considered the interaction of CO_2 with stoichiometric perfection and the oxygen vacancy defect of Zn_2GeO_4 (010) and (001) surfaces using density functional theory. The surface structure, the most stable adsorption mode and adsorption energies, as well as the LDOS and the potential energy profiles for the dissociation of CO_2 on the defective Zn_2GeO_4 surfaces were systematically analyzed. Our main findings are as follows:

(1) For the perfect (010) surface, the active sites $Ge_{3c\text{-}1}$−$O_{3c\text{-}2}$ and $Ge_{3c\text{-}1}\cdots O_{2c\text{-}2}$ interact with the CO_2 molecule leading to a bidentate carbonate species, with adsorption energies being −0.91 and −1.04 eV, respectively. For the perfect (001) surface, the active site Ge_{3c}−$O_{2c}\cdots Ge_{3c}$ interact with the CO_2 molecule leading to a bridged carbonate-like species and result in an adsorption energy of −1.12 eV. Analysis of the LDOS and Mulliken charge for all adsorbed CO_2 on perfect Zn_2GeO_4 surfaces shows that CO_2 accepted electrons from the surface and formed a partially and negatively charged $CO_2^{\delta-}$ species.

(2) For defective Zn_2GeO_4 surfaces, surface oxygen defects were found to play an important role and can significantly influence the interaction of CO_2 with the surface: the oxygen vacancies are the active sites on the defective Zn_2GeO_4 surfaces; the nearby oxygen vacancies can significantly enhance the adsorption energy of CO_2 molecule compared to the perfect surfaces; CO_2 can not only be activated, but can also be further dissociated into CO and O on the surface oxygen defect site, and the oxygen vacancy defect can be healed by the oxygen atom released during the dissociation process.

(3) Through analysis of the dissociative adsorption mechanism of CO_2 on defective Zn_2GeO_4 surfaces, we concluded that CO_2 dissociation on the defective Zn_2GeO_4 (010) surface was thermodynamically preferred and dissociation on the defective Zn_2GeO_4 (001) surface was kinetically preferred. The dissociative adsorption of CO_2 favors the stepwise dissociation mechanism, and the dissociation process can be described as $CO_2 + Vo \rightarrow CO_2^{\delta-}/Vo \rightarrow CO_{adsorbed} + O_{surface}$.

In summary, our results demonstrate that the surface structure of the Zn_2GeO_4 is important for CO_2 adsorption and activation. Oxygen vacancies are found to significantly modify the adsorption properties of CO_2 on Zn_2GeO_4 surfaces, and hence are anticipated to play an important role in CO_2 photoreduction. This result is very important for further experimental investigations and applications in photocatalysis.

■ ASSOCIATED CONTENT

Supporting Information

Adsorption energies, structural parameters, and Mulliken charges for the different CO_2 adsorption configurations, oxygen vacancy formation energy, and optimized different binding configurations and energetics of CO_2 adsorbed on perfect and defective Zn_2GeO_4 (010) and (001) surfaces. This material is available free of charge via the Internet at http://pubs.acs.org.

dx.doi.org/10.1021/la301679h | *Langmuir* 2012, 28, 10415−10424

AUTHOR INFORMATION

Corresponding Author

*Tel: 86-531-88366330, Fax: 86-531-88364864, E-mail: zhaoxian@icm.sdu.edu.cn, fwl@sdu.edu.cn.

Notes

The authors declare no competing financial interest.

ACKNOWLEDGMENTS

This work is supported by the National Natural Science Foundation of China (Grant No. 51172127, 21173131, and 91022034), Excellent Youth Foundation of Shandong Scientific Committee (Grant No. JQ201015), Youth Scientist (Doctoral) Foundation of Shandong Province of China (Grant No. BS2009CL038), and Independent Innovation Foundation of Shandong University (Grant No. 2012TS212). Thanks to Dr. Edward C. Mignot, Shandong University, for linguistic advice.

REFERENCES

(1) Henry, C. R. Surface studies of supported model catalysts. *Surf. Sci. Rep.* **1998**, *31*, 231−325.

(2) Li, Y.; Liu, Q. Y.; Shen, W. J. Morphology-dependent nanocatalysis: metal particles. *Dalton Trans.* **2011**, *40*, 5811−5826.

(3) Xie, X.; Shen, W. Morphology control of cobalt oxide nanocrystals for promoting their catalytic performance. *Nanoscale* **2009**, *1*, 50−60.

(4) Burda, C.; Chen, X. B.; Narayanan, R.; El-Sayed, M. A. Chemistry and properties of nanocrystals of different shapes. *Chem. Rev.* **2005**, *105*, 1025−1102.

(5) Hoffmann, M. R.; Martin, S. T.; Choi, W.; Bahnemann, D. W. Environmental applications of semiconductor photocatalysis. *Chem. Rev.* **1995**, *95*, 69−96.

(6) Linsebigler, A. L.; Lu, G. Q.; Yates, J. T. Photocatalysis on TiO_2 surfaces: principles, mechanisms, and selected results. *Chem. Rev.* **1995**, *95*, 735−758.

(7) Houghton, J. Global warming. *Rep. Prog. Phys.* **2005**, *68*, 1343−1403.

(8) Karl, T. R.; Trenberth, K. E. Modern global climate change. *Science* **2003**, *302*, 1719−1723.

(9) Liu, Q.; Zhou, Y.; Kou, J. H.; Chen, X. Y.; Tian, Z. P.; Gao, J.; Yan, S. C.; Zou, Z. G. High-yield synthesis of ultralong and ultrathin Zn_2GeO_4 nanoribbons toward improved photocatalytic reduction of CO_2 into renewable hydrocarbon fuel. *J. Am. Chem. Soc.* **2010**, *132*, 14385−1487.

(10) Centi, G.; Perathoner, S. Opportunities and prospects in the chemical recycling of carbon dioxide to fuels. *Catal. Today* **2009**, *148*, 191−205.

(11) Indrakanti, V. P.; Kubicki, J. D.; Schobert, H. H. Photoinduced activation of CO_2 on Ti-based heterogeneous catalysts: Current state, chemical physics-based insights and outlook. *Energy Environ. Sci.* **2009**, *2*, 745−758.

(12) Mukherji, A.; Marschall, R.; Tanksale, A.; Sun, C.; Smith, S. C.; Lu, G. Q.; Wang, L. Z. N-doped $CsTaWO_6$ as a new photocatalyst for hydrogen production from water splitting under solar irradiation. *Adv. Funct. Mater.* **2011**, *21*, 126−132.

(13) Zou, Z. G.; Ye, J. H.; Sayama, K.; Arakawa, H. Direct splitting of water under visible light irradiation with an oxide semiconductor photocatalyst. *Nature* **2001**, *414*, 625−627.

(14) Inoue, T.; Fujishima, A.; Konishi, S.; Honda, K. Photoelectrocatalytic reduction of carbon dioxide in aqueous suspensions of semiconductor powders. *Nature* **1979**, *277*, 637−638.

(15) Dimitrijevic, N. M.; Vijayan, B. K.; Poluektov, O. G.; Rajh, T.; Gray, K. A.; He, H.; Zapol, P. Role of water and carbonates in photocatalytic transformation of CO_2 to CH_4 on titania. *J. Am. Chem. Soc.* **2011**, *133*, 3964−3971.

(16) Ma, B. J; Wen, F. Y; Jiang, H. F.; Yang, J. H.; Ying, P. L.; Li, C. The synergistic effects of two co-catalysts on Zn_2GeO_4 on photocatalytic water splitting. *Catal. Lett.* **2010**, *134*, 78−86.

(17) Pan, Y. X.; Liu, C. J.; Mei, D. H.; Ge, Q. F. Effects of hydration and oxygen vacancy on CO_2 adsorption and activation on β-Ga_2O_3(100). *Langmuir* **2010**, *26*, 5551−5558.

(18) Pan, Y. X.; Liu, C. J.; Ge, Q. F. Adsorption and protonation of CO_2 on partially hydroxylated γ-Al_2O_3 surfaces: A density functional theory study. *Langmuir* **2008**, *24*, 12410−12419.

(19) Wang, S. G.; Gao, D. B.; Li, Y. W.; Wang, J. G.; Jiao, H. J. Chemisorption of CO_2 on nickel surfaces. *J. Phys. Chem. B* **2005**, *109*, 18956−18963.

(20) Wang, S. G.; Liao, X. Y.; Cao, D. B.; Huo, C. F.; Li, Y. W.; Wang, J. G.; Jiao, H. J. Factors controlling the interaction of CO_2 with transition metal surfaces. *J. Phys. Chem. C* **2007**, *111*, 16934−16940.

(21) De la Pena O'Shea, V. A.; Gonzalez, S.; Illas, F.; Fierro, J. L. G. Evidence for spontaneous CO_2 activation on cobalt surfaces. *Chem. Phys. Lett.* **2008**, *454*, 262−268.

(22) Payne, M. C.; Teter, M. P.; Allan, D. C.; Arias, T. A.; Joannopoulos, J. D. Iterative minimization techniques for ab initio total-energy calculations: molecular dynamics and conjugate gradients. *Rev. Mod. Phys.* **1992**, *64*, 1045−1097.

(23) Perdew, J. P.; Chevary, J. A.; Vosko, S. H.; Jackson, A. K.; Pederson, R. M.; Singh, D. J.; Fiolhais, C. Atoms, molecules, solids, and surfaces: Applications of the generalized gradient approximation for exchange and correlation. *Phys. Rev. B* **1992**, *46*, 6671−6687.

(24) Perdew, J. P.; Wang, Y. Accurate and simple analytic representation of the electron-gas correlation energy. *Phys. Rev. B* **1992**, *45*, 13244−13249.

(25) Segall, M.; Lindan, P.; Probert, M.; Pickard, C.; Hasnip, P.; Clark, S.; Payne, M. First-principles simulation: ideas, illustrations and the CASTEP code. *J. Phys.: Condens. Matter* **2002**, *14*, 2717−2744.

(26) Vanderbilt, D. Soft self-consistent pseudopotentials in a generalized eigenvalue formalism. *Phys. Rev. B* **1990**, *41*, 7892−7895.

(27) Monkhorst, H. J.; Pack, J. D. Special points for Brillouin-zone integrations. *Phys. Rev. B* **1976**, *13*, 5188−5192.

(28) Halgren, T. A.; Lipscomb, W. N. The synchronous-transit method for determining reaction pathways and locating molecular transition states. *Chem. Phys. Lett.* **1977**, *49*, 225−232.

(29) Freund, H. J.; Roberts, M. W. Surface chemistry of carbon dioxide. *Surf. Sci. Rep.* **1996**, *25*, 225−273.

(30) Mulliken, R. S. Electronic population analysis on LCAOMO molecular wave functions. I. *J. Chem. Phys.* **1955**, *23*, 1833−1840.

(31) Piskunov, S.; Heifets, E.; Eglitis, R. I.; Borstel, G. Bulk properties and electronic structure of $SrTiO_3$, $BaTiO_3$, $PbTiO_3$ perovskites: an ab initio HF/DFT study. *Comput. Mater. Sci.* **2004**, *29*, 165−178.

(32) Liu, J. W.; Chen, G.; Li, Z. H.; Zhang, Z. G. Electronic structure and visible light photocatalysis water splitting property of chromium-doped $SrTiO_3$. *J. Solid State Chem.* **2006**, *179*, 3704−3708.

(33) Huang, J.; Ding, K.; Hou, Y.; Wang, X.; Fu, X. Synthesis and photocatalytic activity of Zn_2GeO_4 nanorods for the degradation of organic pollutants in water. *ChemSusChem* **2008**, *1*, 1011−1019.

(34) Oviedo, J.; Gillan, M. J. The energetics and structure of oxygen vacancies on the SnO_2 (110) surface. *Surf. Sci.* **2000**, *467*, 35−48.

(35) Hu, P.; King, D. A.; Crampin, S.; Lee, M. H.; Payne, M. C. Gradient corrections in density functional theory calculations for surfaces: CO on Pd{110}. *Chem. Phys. Lett.* **1994**, *230*, 501−506.

(36) Chen, H. L.; Chen, H. T.; Ho, J. J. Density functional studies of the adsorption and dissociation of CO_2 molecule on Fe(111) surface. *Langmuir* **2010**, *26*, 775−781.

(37) Bork, N.; Bonanos, N.; Rossmeisl, J.; Vegge, T. Ab initio charge analysis of pure and hydrogenated perovskites. *J. Appl. Phys.* **2011**, *109*, 033702−1−4.

(38) Rasko, J.; Solymosi, F. Infrared spectroscopic study of the photoinduced activation of CO_2 on TiO_2 and Rb/TiO_2 catalysts. *J. Phys. Chem.* **1994**, *98*, 7147−7152.

(39) Wang, Y.; Lafosse, A.; Jacobi, K. Adsorption and reaction of CO_2 on the RuO_2 (110) surface. *J. Phys. Chem. B* **2002**, *106*, 5476−5482.

(40) Campbell, C. T.; Peden, C. H. F. Oxygen vacancies and catalysis on ceria surfaces. *Science* **2005**, *309*, 713−714.
(41) Lee, J.; Sorescu, D. C.; Deng, X. Electron-induced dissociation of CO_2 on TiO_2 (110). *J. Am. Chem. Soc.* **2011**, *133*, 10066−10069.
(42) Indrakanti, V. P.; Kubicki, J. D.; Schobert, H. H. Photoinduced activation of CO_2 on TiO_2 surfaces: Quantum chemical modeling of CO_2 adsorption on oxygen vacancies. *Fuel Process. Technol.* **2011**, *92*, 805−811.
(43) He, H. Y.; Zapol, P.; Curtiss, L. A. A Theoretical study of CO_2 anions on anatase (101) surface. *J. Phys. Chem. C* **2010**, *114*, 21474−21481.
(44) Pipornpong, W.; Wanbayor, R.; Ruangpornvisuti, V. Adsorption CO_2 on the perfect and oxygen vacancy defect surfaces of anatase TiO_2 and its photocatalytic mechanism of conversion to CO. *Appl. Surf. Sci.* **2011**, *257*, 10322−10328.